ARTICLE IN PRESS

Nature Communications

https://doi.org/10.1038/s41467-026-73151-8

Article in Press

Long-range electronic interactions of tubular single-atom Cu-N_3 catalysts for nanoconfined direct electron transfer oxidation

Received: 7 May 2025

Accepted: 30 April 2026

Cite this article as: Yan, H., Li, B., Liu, S. *et al.* Long-range electronic interactions of tubular single-atom Cu-N_3 catalysts for nanoconfined direct electron transfer oxidation. *Nat Commun* (2026). https://doi.org/10.1038/s41467-026-73151-8

Huchuan Yan, Bisheng Li, Shiyu Liu, Mingzhu Zhou, Xuerong Zhou, Dengsheng Ma, Dongbo Wang, Hongjun Lin, Xiaoguang Duan & Cui Lai

We are providing an unedited version of this manuscript to give early access to its findings. Before final publication, the manuscript will undergo further editing. Please note there may be errors present which affect the content, and all legal disclaimers apply.

If this paper is publishing under a Transparent Peer Review model then Peer Review reports will publish with the final article.

ARTICLE IN PRESS

© The Author(s) 2026. **Open Access** This article is licensed under a Creative Commons Attribution-NonCommercial-NoDerivatives 4.0 International License, which permits any non-commercial use, sharing, distribution and reproduction in any medium or format, as long as you give appropriate credit to the original author(s) and the source, provide a link to the Creative Commons licence, and indicate if you modified the licensed material. You do not have permission under this licence to share adapted material derived from this article or parts of it. The images or other third party material in this article are included in the article's Creative Commons licence, unless indicated otherwise in a credit line to the material. If material is not included in the article's Creative Commons licence and your intended use is not permitted by statutory regulation or exceeds the permitted use, you will need to obtain permission directly from the copyright holder. To view a copy of this licence, visit http://creativecommons.org/licenses/by-nc-nd/4.0/.

Long-range electronic interactions of tubular single-atom Cu-N_3 catalysts for nanoconfined direct electron transfer oxidation

Huchuan Yan[1,†], Bisheng Li[2,†], Shiyu Liu[1], Mingzhu Zhou[2], Xuerong Zhou[1], Dengsheng Ma[1], Dongbo Wang[1], Hongjun Lin[2*], Xiaoguang Duan[3*], Cui Lai[1*]

[1] College of Environmental Science and Engineering, Hunan University and Key Laboratory of Environmental Biology and Pollution Control (Hunan University), Ministry of Education, Changsha 410082, Hunan, China.

[2] College of Geography and Environmental Sciences, Zhejiang Normal University, Jinhua 321004, China.

[3] School of Chemical Engineering, Adelaide University, Adelaide, SA 5005, Australia.

[†] These authors contributed equally to this work.

*Corresponding authors: Cui Lai, laicui@hnu.edu.cn; Xiaoguang Duan, xiaoguang.duan@adelaide.edu.au; Hongjun Lin, hjlin@zjnu.cn.

Abstract

Leveraging atomically dispersed catalysts to selectively trigger nonradical oxidation can overcome the short lifetimes and poor selectivity of radical-based processes in water treatment. Here, we integrate long-range electronic modulation with nanoconfinement by embedding isolated Cu-N_3 sites into carbon-doped tubular carbon nitride (CuTCN/C). Carbon atoms intrinsic to the support upshift the Cu *d*-band center, which strengthens peroxymonosulfate (PMS) adsorption and lowers the activation energy barrier. Moreover, surface mesopores greatly enrich local PMS concentration in the nanoconfined environment and accelerate interfacial electron migration to coordinate a direct electron transfer pathway. As a result, CuTCN/C delivers the highest activity among Cu single-atom catalysts, while operating with minimal PMS doses due to the remarkably accelerated mass transfer. Spectroscopic, electrochemical, DFT and MD analyses confirm the synergistic roles of electronic tuning and nanoconfinement in promoting oriented PMS activation as reactive surface complex that directly attacks surface-enriched pollutants with high PMS utilization efficiency. The continuous fluidized-bed tests demonstrate strong salt tolerance and long-term stability of the system, while life-cycle assessment confirms favorable environmental metrics in practical application. This dual engineering strategy of macroscopic morphological and microscopic electronic structure provides a blueprint for smart design of robust single-atom catalysts for selective and high-efficiency water purification.

Keywords: Single-atom catalysts; Electron transfer pathway; Nanoconfinement; Electronic structure modulation; Water purification

Introduction

With urbanization and industrialization, the scarcity of clean water resources is becoming a critical challenge[1,2]. Developing environmentally friendly, low-cost, and efficient water treatment technologies is critically required. Notably, advanced oxidation processes (AOPs) targeting in situ degradation and mineralization of organic pollutants is an excellent option[3,4]. However, conventional AOPs primarily rely on radicals such as $SO_4^{\bullet-}$ and $HO^{\bullet}$, which suffer from limitations including low selectivity in decontamination and vulnerability to interference from inorganic anions. In contrast, non-radical pathways demonstrate strong anti-interference capabilities in complex water matrices, reducing unnecessary consumption of catalysts and oxidants while preventing the formation of more toxic disinfection by-products[5,6]. Among these non-radical pathways, the electron transfer pathway (ETP) has gained significant attention due to its half-life-independent nature and rapid kinetic[7-9]. Therefore, advancing ETP-based Fenton-like technologies holds significance.

Single-atom catalysts (SACs), recognized as one of the most promising catalysts, possess exceptional atom utilization, tunable electronic structures, and outstanding selectivity[10-12]. To date, various SACs have been designed and used to activate peroxymonosulfate (PMS), enabling efficient degradation of pollutants via ETP[13-15]. Notably, SACs applied in industrial catalysis must not only require strong anti-interference capability and selectivity but also demand long-term stability and exceptional catalytic activity[16,17]. A critical challenge arises from the strong interaction between metal active centers and reaction intermediates, leading to catalytic site blockage and eventual deactivation, which compromises both catalytic activity and stability[18]. To address this limitation, substantial studies have focused on modifying SACs by tailoring the number and elements of coordination atoms in first shell layer (FSL) surrounding metal atoms[19-21]. However, strategies of regulating second or higher-shell coordination environment (e.g., long-range electronic coupling) are relatively few, despite also having the ability to improve various performance of SACs. For example, Wu et al. explored that topological defects can regulate the *d*-band characteristics of nearby Fe-N_4 sites, enhancing both activity and stability of Fe SACs in Fenton-like reactions[22]. Zhang et al. introduced S heteroatoms into a high-coordination shell of Fe SACs, inducing long-range interactions that altered the electronic structure of Fe sites and significantly improved catalytic activity[23]. Thus, precisely manipulating distal species holds scientific feasibility and exploratory potential for improving the fine-tuning the reactivity of SACs.

Heteroatom doping is a common strategy for modulating the second or higher-shell coordination environment of SACs, which may induce changes in the electronic features of metal active sites (e.g., *d*-band center position, charge density distribution) [24]. Current research primarily focuses on doping heteroatoms with pronounced electronegativity differences from the substrate, such as S, O, and B, while the catalytic behavior of SACs doped with elements identical to the support remains unknown[25-27]. Moreover, given the inherent limitations of SACs, such as limited exposure of active metal sites and restricted mass transport, deliberate design of confined spaces to enhance the local concentration of reactants can not only improve pollutant degradation kinetics but also reduce the required dosage of chemical reagents[28,29]. In PMS-AOPs, both high-shell electronic modulation and nanoconfinement strategies have been explored independently for SACs[30,31]. However, the simultaneous regulation of long-range interactions and confinement effects in SACs to meet practical applications across has rarely been reported, leading to insufficient understanding of their structure-property relationships.

In this work, nanoconfined tubular CN (TCN) was synthesized using a supramolecular self-assembly method, and the electronic structure of Cu-N_3 site was modulated by integrating carbon atoms into TCN substrates during the preparing Cu SACs (CuTCN/C). Subsequently, the morphology, chemical state, and atomic structure of CuTCN/C were characterized, and the effect of the Cu centers properties and confined space on Fenton-like catalytic activity were systematically evaluated. Based on experiments and theoretical calculation, the primary active sites and direct ETP mechanism were elucidated. Furthermore, the high activity, stability, and environmental adaptability of CuTCN/C were demonstrated by life cycle assessment, long-term fluidized-bed reactor experiments and experiments on the effects of various environmental factors.

Results

Nano-confinement and carbon-doped engineering of CuTCN/C

Cu SACs anchored on hollow carbon-doped TCN were prepared by one-step pyrolysis (Fig. 1a). Typically, melamine was selected as a building unit, which decomposes into cyanuric acid and then forms rod-like precursor during hydrothermal process. The rod-like precursor was further calcined to transform into microtubular CN while urea was decomposed into ammonia gas to create holes in the tubular at 550°C[32]. Subsequently, TCN was homogeneously mixed with cupric acetylacetonate and the CuTCN/C catalyst was obtained after pyrolyzing the mixture under an Ar atmosphere. Control samples, referred to as CuBCN/C and CuTCN, were prepared through similar steps, but with different CN and Cu sources adopted, respectively. The pore size distribution curves uncover that CuTCN/C is predominantly characterized by well-defined mesopores centered at 2.0 nm, whereas CuBCN/C displays a broader pore size distribution range without a distinct dominant pore size (Supplementary Fig. 1). Likewise, CuTCN/C possesses the highest specific surface area of 64.11 m^2g^{-1} (Supplementary Table 1).

The scanning electron microscopy (SEM) characterization reveals that CuTCN/C exhibits a tubular morphology, whereas CuBCN/C exhibits a bulk structure (Fig. 1g-j and Supplementary Fig. 2). Transmission electron microscopy (TEM) images do not reveal the presence of Cu nanoparticles in CuTCN/C (Fig. 1k-m). Meanwhile, the selected area electron diffraction (SAED) pattern of CuTCN/C further rules out the presence of Cu crystals (Fig. 1n). The energy dispersive spectrometer (EDS) mapping indicates a homogeneous distribution of C, N, O, and Cu throughout the sample (Fig. 1b-f). The Cu contents was quantified by inductively coupled plasma emission spectrometer measurement to be 11.0 wt%. To demonstrate that Cu is distributed in the atomic form, aberration-corrected high-angle dark-field scanning TEM (HAADF-STEM) measurement was adopted. Fig. 1o and p highlight bright dots representing the atomic-sized Cu atoms, encircled in red. The X-ray diffraction (XRD) pattern of CuTCN/C exhibits a single prominent characteristic peak at approximately 27.6°, which is consistent with the structure to TCN[33]. The absence of additional peaks represents that no Cu crystals are formed, aligning with the SAED results (Supplementary Fig. 3). The Fourier transform infrared (FTIR) analysis indicates that CuTCN/C and TCN share comparable functional groups (Supplementary Fig. 4)[34]. However, the peaks of CuTCN/C at 1200-1750 cm^{-1} corresponding to C-N heterocycles have some slight variations, which may be due to the partial substitution of N by C[35].

Chemical state analysis and atomic structure of CuTCN/C

The chemical states of CuTCN/C catalysts were examined using X-ray photoelectron spectroscopy (XPS). The C 1*s* spectrum of CuTCN/C is deconvolved into four components at 284.80, 286.19, 287.89, and 288.92 eV, which correspond to C=C, C-C, N-C=C, and C=N/C=O, respectively (Supplementary Fig. 5a)[36]. As the cupric acetylacetonate content in the precursor rises, the proportion of C=C and C-C increases, with C=C comprising 36.4% in CuTCN/C-0.1 and 49.3% in CuTCN/C (Supplementary Table 2). A similar trend is observed, where the N-$(C)_3$ content in N 1*s* spectra increases as the amount of cupric acetylacetonate increases (Supplementary Table 3 and Supplementary Fig. 5b) [37]. XPS analysis uncovers that the ratios of C/N in CuTCN/C-0.1 and CuTCN/C are 1.17 and 1.77, respectively. Meanwhile, C *K*-edge X-ray absorption near-edge structure (XANES) spectra reveal that CuTCN/C not only retains the π* C-C/C=C and π* C-N-C absorption peaks typical of traditional CN, but also exhibits a new C-C peak at approximately 293 eV (Supplementary Fig. 6)[38]. To sum up, cupric acetylacetonate serves as both copper and carbon precursors, integrating carbon atoms into the TCN framework.

In the Cu 2*p* spectrum, the binding energies at 932.24 and 951.93 eV are attributed to Cu^+, which is further confirmed by Cu LMM Auger spectrum (Fig. 2a)[39]. In addition, the characteristic peaks of Cu^{2+} appear at 934.79 and 954.60 eV, respectively[40]. This observation shows a good agreement with the Cu *K*-edge extended XANES spectra. As shown in Fig. 2b, the absorption edge position of CuTCN/C lies between Cu_2O and CuO, suggesting that the Cu valence state ranging from +1 and +2. To gain further insights into the microenvironment of Cu species in CuTCN/C, X-ray absorption spectra was adopted. The Fourier transform (FT) extended X-ray absorption fine structure (EXAFS) of CuTCN/C display prominent peaks at 1.38 Å and 2.36 Å, corresponding to Cu-N and Cu-N-C bonds in the first and second coordination shells, respectively (Fig. 2c). The wavelet transform (WT) analysis confirms the above result, showing Cu-N and Cu-N-C signals in CuTCN/C matched well with CuPc (Fig. 2e-i)[41]. Furthermore, EXAFS fitting reveals an average Cu-N coordination number is 3.1 (Fig. 2d and Supplementary Table 4). As a control sample, CuBCN/C displays an identical coordination environment to that of CuTCN/C, with a Cu-N coordination number of 3.0 (Supplementary Fig. 7 and Supplementary Table 4).

Activity of catalysts under dual regulation

Three transition metal SACs (Fe, Co, Cu) were synthesized using identical preparation methods to systematically evaluate their capabilities in forming ETP within the PMS system. Comparative analysis of the Gibbs free energy profiles for ETP formation revealed that CuTCN/C exhibits the lowest energy barrier in the rate-determining step, followed by FeTCN/C and CoTCN/C (Supplementary Fig. 8a). These computational results demonstrate the superior ETP performance of CuTCN/C, which is consistent with our experimental observations (Supplementary Fig. 8b). Based on these findings, CuTCN/C was selected as the optimal candidate for subsequent mechanistic investigations. To explore the effects of nanoconfinement and the carbon heteroatom-induced electronic structure regulation of Cu centers on tuning Fenton-like reaction activity, the removal efficiency of acetaminophen (ACE) was examined by activating PMS. Compared to the meager reactivity of TCN and carbon doped TCN (TCN/C), introducing Cu single atoms greatly enhances catalytic performance (Supplementary Fig. 9). Inductively coupled plasma mass spectrometry analysis confirmed negligible Cu ions leaching from the CuTCN/C+PMS system (only 0.016 mg/L for CuBCN/C+PMS), ruling out the contribution from homogeneous Cu ions to PMS activation (Supplementary Fig. 10). Additionally, when oxalic acid was used as a chelating agent to mask Cu active sites, the degradation of ACE in the CuTCN/C+PMS system is severely inhibited. The above results confirm the role of Cu single-atoms as critical active sites enabling PMS activation. Then, the catalytic performance of Cu single-atoms loaded on different CN substrates (carbon doped bulk CN (BCN/C), TCN, and TCN/C) was compared. As shown in Fig. 3a, only about 41.9% and 8.6% ACE are removed by CuBCN/C and CuTCN catalyst, respectively. However, the CuTCN/C catalyst achieves the complete removal of ACE, suggesting that both nanoconfinement and carbon atoms doping within the CN structure synergistically enhance catalytic activity. Furthermore, the ACE removal efficiency in the CuTCN/C+PMS system is obviously higher compared to that achieved with CuTCN/C or PMS alone, underscoring the superior catalytic efficiency of the Fenton-like reaction. Notably, CuTCN/C also exhibited excellent catalytic activity toward peroxydisulfate (PDS) activation (Supplementary Fig. 10). To further evaluate ACE removal, the total organic carbon (TOC) removal rate of CuTCN/C+PMS system post-reaction was assessed. Impressively, CuTCN/C+PMS system achieved 25.9% TOC removal within just 10 min, significantly outperforming the CuBCN/PMS+PMS system (8.6%) . Meanwhile, the potential degradation intermediates of ACE were identified and proposed (Supplementary Fig. 11). The calculated reaction rate constants for ACE removal using CuTCN/C, CuBCN/C, and CuTCN are approximately 0.966 min^{-1}, 0.050 min^{-1}, and 0.007 min^{-1}, respectively. The turnover frequency (TOF) of CuTCN/C was calculated as 0.084 min^{-1}, nearly 4.0 and 19.5 times higher than those of CuBCN/C and CuTCN, respectively (Supplementary Table 5). In contrast to most cutting-edge catalysts, CuTCN/C catalyst demonstrates remarkable catalytic performance (Supplementary Table 6). The optimization experiments of PMS concentration and CuTCN/C dosage show that ACE removal increases with increasing CuTCN/C dosage (Supplementary Fig. 12a). Nevertheless, the optimal concentration of PMS is determined to be 0.2 mM, beyond which further increases in PMS usage do not significantly enhance ACE removal efficiency (Supplementary Fig. 12b). Notably, achieving efficient ACE removal at such a low PMS concentration offers dual benefits in terms of minimizing chemical input and reducing the residual SO_4^{2-} generation, making the process more economical and environmentally sustainable.

Direct electron transfer-driven pollutant removal mechanism

The pivotal active species in CuTCN/C+PMS system were determined through a series of quenching experiments. The addition of excess methanol (MeOH) and tert-butyl alcohol (TBA), which acts as scavengers for $SO_4^{\bullet-}$ and $HO^{\bullet}$, resulted in minimal inhibition of ACE removal, indicating that these radicals contributed negligibly to the reaction (Fig. 3b and Supplementary Fig. 13a). Similarly, furfuryl alcohol (FFA) addition also does not cause evident suppression in CuTCN/C+PMS system, manifesting that almost no $^1O_2$ is generated. The $O_2^{\bullet-}$ was not probed relevant in this context, as it has been proven not to directly react with ACE[42]. Besides, benzoic acid (BA), nitrobenzene (NB), and metronidazole (MDE) were used as probes to identify and quantify the concentration of $SO_4^{\bullet-}$, $HO^{\bullet}$, and $^1O_2$, respectively. The results indicate negligible generation of $SO_4^{\bullet-}$, $HO^{\bullet}$, and $^1O_2$ (Supplementary Fig. 13b). The electron paramagnetic resonance (EPR) analysis further confirms that $SO_4^{\bullet-}$ and $HO^{\bullet}$ are not present (Fig. 3c). The spin-trap reagent 2,2,6,6-tetramethyl-4-piperidinol (TEMP) reveals a weak TEMP-$^1O_2$ signal in PMS and CuTCN/C+PMS systems. In comparison with PMS alone, TEMP-$^1O_2$ peak intensity remains almost unchanged after adding CuTCN/C, indicating that CuTCN/C is unable to activate PMS to produce $^1O_2$. Furthermore, hydrophobic phenol, used as a scavenger of surface-bound radicals, caused little inhibition of CuTCN/C activity and negligible phenol consumption, eliminating the role of surface-bound radicals[43] (Fig. 3b and Supplementary Fig. 14). The phenyl methyl sulfoxide (PMSO) was employed to detect high-valent copper-oxo species to form the specific product of phenyl methyl sulfone ($PMSO_2$) via oxygen transfer pathway. The results demonstrate negligible PMSO consumption and $PMSO_2$ formation, indicating the absence of high-valent copper-oxo species (Supplementary Fig. 15).

With the exclusion of the previously discussed active species, the electron transfer path was investigated. In situ Raman spectroscopy was adopted to monitor the surface chemical evolution of CuTCN/C up PMS addition. A new peak emerges at ~832 cm^{-1}, corresponding to activated PMS (PMS*), while no Cu(III) peak appears[44,45] (Fig. 3d). Subsequently, the addition of ACE results in the observed disappearance of PMS*. Moreover, the in situ FTIR spectra reveal a distinct red shift upon the addition of CuTCN/C compared to PMS, indicating the formation of surface bonding between PMS and CuTCN/C (Fig. 3e). The effect of high ionic strength on ACE removal efficiency also supported the above findings, showing that 100 mM $NaClO_4$ has no evident effect on ACE removal (Supplementary Fig. 16), confirming the strong interaction between PMS and CuTCN/C (i.e., an inner-sphere reaction). Meanwhile, the PMS consumption within 10 min increased significantly from 9.3% to 64.2% upon ACE addition, providing strong evidence for the electron transfer path in the CuTCN/C+PMS system (Supplementary Fig. 17). To further confirm that electron transfer pathway is the primary mechanism for oxidation, electrochemical assays were employed[46,47]. Specially, the open-circuit potential (OCP) of CuTCN/C-coated electrode rises sharply upon PMS addition and then potential rebounds upon ACE injection, suggesting that of the formation and pollutant-related consumption of surface-activated PMS complex (Fig. 3f)[48]. Subsequently, chronoamperometry (CA) tests were performed, using both the initial voltage (0.24V) of the CuTCN/C-coated electrode and the maximum voltage after PMS injection (0.62V) as the applied constant voltages. As shown in Fig. 3g, no evident current response is observed with or without ACE at 0.24 V. However, at 0.62 V, which exceeds the oxidation potential of ACE (0.50V), the current response in the presence of ACE is markedly higher than that without ACE, confirming the occurrence of electron transfer between PMS* and ACE (Supplementary Fig. 18)[49].

Meanwhile, the selectivity of electron transfer pathway with a mild oxidation capacity was utilized to investigate the degradation ability of CuTCN/C toward various electron-rich and electron-deficient pollutants (Supplementary Fig. 19). The results indicate that the CuTCN/C+PMS system selectively degraded electron-rich pollutants (aminophenol, ACE, p-methoxyphenol, etc.) while being less effective at degrading electron-deficient pollutants (benzoic acid), further demonstrating the dominant role of the electron transfer pathway. Additionally, given the weak catalytic activity of CuTCN, comparisons of the PMS activation mechanism were conducted only between the CuBCN/C catalyst, which demonstrates a certain level of catalytic activity, and the CuTCN/C catalyst. Masking experiments, PMS consumption tests, probe experiment, and electrochemical analyses consistently confirmed that the CuBCN/C+PMS system also predominantly follows an electron transfer mechanism, indicating that nanoconfinement does not alter the catalytic behavior of Cu-N_3 sites (Supplementary Figs. 20 and 21).

Notably, electron transfer pathways can be categorized into two distinct types: the direct electron transfer path (DETP), in which electrons flow directly from the contaminant to PMS*, and the catalyst-mediated electron transfer path (CMETP), where the contaminant donates electrons that are subsequently transferred to PMS* via catalyst (Supplementary Fig. 22). To distinguish the two pathways, galvanic oxidation system (GOS) was adopted. The GOS separates PMS and ACE into two chambers, and CuTCN/C-coated graphite flake is used as electrodes to preclude direct reaction of PMS* with ACE (Supplementary Fig. 23a). If the primary mechanism is CMETP rather than DETP, electrons can still be transferred from ACE to PMS via the electron channel, enabling ACE degradation. However, no significant ACE removal is detected in two-chamber reaction systems (Supplementary Fig. 23b). In contrast, in a single-compartment system where the graphite electrode coated with CuTCN/C immersed in a solution containing PMS and ACE, effective degradation of ACE is observed (Supplementary Fig. 24). These findings indicate that DETP plays a dominant role in CuTCN/C+PMS system, distinct from the traditional CMETP observed in most carbon-based materials. This divergence likely arises from differences in the electrical conductivity of catalyst supports and/or their distinct adsorption/activation behaviors toward reactants (organic substrates and oxidants)[8]. Specifically, CN exhibits semiconductor properties with inferior conductivity, making it difficult to mediate electron transfer through the CN substrate. In contrast, traditional carbon substrates such as carbon nanotube (CNT) and graphene possess excellent conductivity that enables efficient electron transport. To validate this hypothesis, we selected high-temperature calcined hollow carbon spheres (HC) and CNT as substrate materials, fabricating CuHC and CuCNT using identical calcination protocols as CuTCN/C. Electrochemical impedance spectroscopy (EIS) revealed enhanced conductivity in both CuHC and CuCNT compared to CuTCN/C (Fig. 4b). Subsequent GOS validation demonstrated that highly conductive CuHC and CuCNT effectively achieved ACE removal in two-chamber configurations, exhibiting fundamentally different behavior from CuTCN/C (Supplementary Fig. 23b). Moreover, CMETP requires the pollutant donate electrons to the catalyst support, while DETP necessitates spatial proximity between PMS and the pollutant. To investigate the structural basis for these pathways, we constructed a computational model of a conventional carbon-based Cu-N_3 single-atom catalyst (CuNC) and analyzed its adsorption behavior toward ACE and PMS, comparing it with that of CuTCN/C. For CuNC, both PMS and ACE can adsorb individually on Cu sites, with adsorption energies of -1.22 eV and -0.69 eV, respectively (Supplementary Fig. 25a). However, their co-adsorption on the same site yields a binding energy of only -1.40 eV, less than the sum of the individual adsorption energies, suggesting thermodynamic infeasibility for their simultaneous binding and spatial separation in the CuNC+PMS+ACE system. In contrast, for CuTCN/C, ACE and PMS exhibit individual adsorption energies of -0.11 eV and -1.00 eV, respectively (Supplementary Fig. 25b). When co-adsorbed, the energy drops to -2.27 eV, indicating strong and favorable simultaneous binding at the same Cu sites, with minimal spatial hindrance.

Charge density difference analyses further support this distinction: while CuNC can engage in electron transfer with ACE or PMS individually, it fails to do so when both are co-adsorbed, favoring CMETP (Supplementary Fig. 26a). Conversely, in CuTCN/C, ACE alone does not readily undergo electron transfer; however, co-adsorption with PMS induces charge redistribution and forms an integrated complex with Cu site, facilitating direct electron transfer between ACE and PMS (Supplementary Fig. 26b). Collectively, these findings demonstrate that CMETP dominates in systems with highly conductive support, where pollutants and oxidants are spatially separated but can interact through the carrier. In contrast, DETP is favored in low-conductivity materials like CuTCN/C, where direct molecular contact between PMS and pollutant via inner-sphere interactions enables efficient and short-range electron transfer at the active site (Fig. 3h).

Nanoconfinement effects and long-range interaction mechanism

In contrast to CuBCN/C, the hydrothermally modified CuTCN/C exhibits a tubular structure with abundant mesopores (2 nm), which not only creates a concave interfacial nano-environment but also confines catalytic reactions within the nanostructure. Comparative analysis of the catalytic performance and activation mechanisms between CuBCN/C and CuTCN/C reveals that CuTCN/C exhibits superior catalytic activity and PMS utilization efficiency, while both share identical catalytic mechanisms. This indicates that the nanoconfinement effect in CuTCN/C effectively accelerates reaction kinetics, as evidenced by comparative studies with two-dimensional flake-like carbon-doped carbon nitride supported copper single-atom catalysts (CuFCN/C), where nanoconfined CuTCN/C possesses the strongest PMS activation capability (Supplementary Fig. 27). Molecular dynamics (MD) simulations show that PMS concentration distributes uniformly in CuBCN/C, whereas CuTCN/C achieves a 2.0-fold enrichment of PMS concentration within its pore channels, displaying significant spatial accumulation (Fig. 4a). Mean square displacement (MSD) analysis further confirms the accelerated PMS reaction-diffusion kinetics under nanoconfinement in CuTCN/C. Furthermore, electrochemical tests corroborate the role of nanoconfinement in modulating electron transfer capabilities. Cyclic voltammetry (CV) curves illustrate that CuTCN/C exhibits the highest current density and superior reductive capacity (Supplementary Fig. 28). EIS suggests that CuTCN/C exhibits enhanced conductivity compared to CuBCN/C (Fig. 4b). Collectively, these findings establish that the spatial confinement in CuTCN/C effectively accelerates electron transfer, facilitates PMS mass transport, and accelerates surface reaction rates.

Subsequently, DFT calculations were conducted to reveal the impact of carbon doping and the mechanism behind DETP formation. According to the characterization results, the corresponding structure models of CuTCN/C and CuTCN were constructed and optimized (Supplementary Fig. 29). The reaction pathways and Gibbs free energy changes associated with Fenton-like reactions on CuTCN and CuTCN/C were calculated according to the DETP mechanism depicted in Fig. 4c. Firstly, PMS is adsorbed onto the Cu-N_3 sites, releasing energy. The adsorbed PMS is then activated, with the dangling -SO_5H and the subsequently generated

-SO_4 group capturing electrons from pollutants, driving oxidative degradation. Finally, -SO_4H group desorbs from the catalyst, allowing the regeneration of Cu-N_3 sites[50]. Encouragingly, after carbon doping modification, CuTCN/C exhibits a lower adsorption free energy compared to CuTCN, indicating a stronger PMS adsorption capacity. Moreover, the rate-determining step (-SO_4H desorption) on CuTCN/C has a significantly lower energy barrier on CuTCN/C, which facilitates its regeneration for continuous PMS activation. These findings are well-supported by experimental results.

The projected density of state (PDOS), charge density difference, and Bader charge analyses reveal that long-distance doped carbon atoms optimize the electronic microenvironment of Cu single atoms. As shown in Figs. 4d and 4e, CuTCN/C exhibits a narrower band gap with moderately enhanced conductivity compared to CuTCN. However, both catalysts exhibit no significant electronic states near the Fermi level, demonstrating characteristic semiconductor behavior with low conductivity. Consequently, the electron of pollutants is difficult to transfer through catalyst-mediated pathways, predominantly following the DETP. In addition, the long-range interactions of the doped carbon atoms on the neighboring Cu-N_3 sites shift *d*-band center of Cu from -1.80 eV to -1.64 eV (Fig. 4g). The upward shift brings the *d*-band center of CuTCN/C closer to the Fermi level, potentially leading to higher catalytic activity, enhanced electron transfer, and a greater PMS adsorption ability[22,51]. Meanwhile, the peaks of C 2*p* and Cu 3*d* in CuTCN/C predominantly resonate and overlap near the Fermi level, indicating that the doped carbon atoms activate the *d*-band electrons of Cu single atoms, further enhancing Cu *d*-band activity[52]. Furthermore, the differences in PDOS between CuTCN and CuTCN/C after PMS adsorption were also investigated. Compared to CuTCN, CuTCN/C exhibits a greater overlap among the doped carbon atoms, Cu site, and the O atom of PMS adsorbed on the Cu site, demonstrating that carbon-doping facilitate their interactions. Moreover, the PDOS results indicate that after PMS adsorption, the *d*-band center of CuTCN shifts upward, while the opposite occurs for CuTCN/C (Fig. 4h). This difference arises from the significant interaction and the transfer of electrons between Cu of CuTCN/C and PMS, which shifts the Cu *d*-band center away from the Fermi level toward a low energy level, thereby enhancing the stability of the CuTCN/C+PMS system[53]. However, for CuTCN, the weaker interaction between Cu and PMS leads to an increase in Cu *d*-band center to high energy level, making the CuTCN+PMS system unstable. Consistent with the PDOS results, charge density difference and Bader charge analysis reveals a more pronounced charge transfer between Cu site and PMS in CuTCN/C involving charge transfer of the doped C in CuTCN/C (Fig. 4i). The Cu in CuTCN/C loses 0.85 e^-, which is higher than the 0.72 e- in CuTCN. The adsorption energy (E_{ads}) results suggest CuTCN/C possesses a stronger binding to PMS (-1.0 eV), whereas CuTCN displays a lower adsorption energy (-0.55 eV). Combined with the correlation among E_{ads}, *d*-band center, and the oxidation capacities (Fig. 4f), the long-range interaction between the doped carbon atoms and Cu single atoms induces the near-Fermi electronic state of Cu-N_3 sites, enhancing the bonding strength with PMS and reaction kinetics.

Performance of CuTCN/C in practical application

Life cycle assessment (LCA) was conducted to evaluate the sustainability and environmental viability of CuTCN/C+PMS system, with comparisons to CuTCN+PMS and

CuBCN/C+PMS systems presented in this study. The assessment considered 18 descriptors commonly associated with modern wastewater treatment processes, including global warming potential, freshwater eutrophication, marine eutrophication, and other significant environmental impacts (Supplementary Tables 7, 8, and Supplementary Fig. 30). As illustrated in Fig. 5a, the CuTCN/C+PMS system exhibited the lowest values across all descriptors, highlighting its superior environmental friendliness. This is because of the superior catalytic activity of CuTCN/C, which reduces the demand for both the catalyst and PMS. Moreover, in practical applications, the reduced consumption of raw materials also lowers transportation costs between production facilities and wastewater treatment plants, thereby further minimizing the system's overall environmental footprint. These findings underscore the potential of CuTCN/C+PMS as a sustainable and efficient solution for wastewater treatment.

In view of the extraordinary properties of CuTCN/C, the possibility of its practical application was further explored. Real water bodies typically contain complex substrates and are subject to diverse environmental conditions, making it essential for CuTCN/C catalyst to be recyclable, stable over time, and resistant to interference. Notably, even after four cycles, ACE is still almost completely removed (Fig. 5b). Furthermore, the catalyst structure remains unchanged after reaction, which proves that it has high stability (Supplementary Figs. 31-33). Meanwhile, the catalytic performance of CuTCN/C also proved robust against variations in environmental factors such as pH, the presence of humic acid (HA), and typical ions (Cl^-, $H_2PO_4^-$, NO_3^-, Ca^{2+}, and Mg^{2+}), maintaining high catalytic activity across diverse conditions (Supplementary Figs. 34-36). To systematically evaluate environmental adaptability, CuTCN/C was tested in two functionally distinct reactor configurations: a stirred-tank reactor simulating natural aquatic systems and a laminar-flow membrane reactor emulating industrial wastewater treatment. This dual-system approach enables rigorous evaluation of catalytic behavior across distinct hydrodynamic regimes and wastewater compositions. For the stirred-tank reactor system, three natural water bodies were selected for evaluation. Remarkably, even with an ultra-low CuTCN/C dosage of 15 mg, the system maintains over 80% ACE removal throughout 20 hours of continuous operation (Supplementary Fig. 37). Scaled-up testing was subsequently conducted (device schematic in Fig. 5c) with authentic ACE-contaminated medical wastewater, revealing exceptional practicality. Continuous operation at 60 mL/h flow rate through the CuTCN/C-functionalized filtration membrane (CuTCN/C@PVDF) achieves consistent ACE elimination (>90%) throughout 200 h of uninterrupted service (Figs. 5c and 5d). The CuTCN/C@PVDF possesses excellent flexibility and elasticty, with SEM imaging revealing both the PVDF membrane structure and the bilayer structure of CuTCN/C loaded onto the PVDF substrate (Figs. 5e-h). Collectively, these results underscore the significant potential of CuTCN/C for practical water decontamination application.

Discussion

To sum up, we developed an innovative Cu SACs anchored on confined carbon-doped TCN that achieves dual modulation of the support morphology and electronic structure. The electronic effect of Cu-N_3 sites, regulated through carbon atoms doping, and the nanoconfinement effects of CuTCN/C were systematically investigated. Both DFT calculations and experimental analyses indicated that long-range carbon atoms effectively changed the PDOS distribution of Cu centers, while the nanoconfinement accelerated electron transfer and enhanced PMS mass transport. The CuTCN/C catalyst exhibited considerable Fenton-like catalytic activity even at a low concentration of PMS, attributed to its optimized nanoconfined morphology and electronic structure. The modulation of the electronic density around the Cu centers enhanced PMS adsorption and facilitated interfacial charge transfer, thereby promoting nonradical activation by forming surface-activated PMS complexes. Meanwhile, CuTCN/C maintained excellent catalytic activity across a wide pH range, under high salinity, and in actual water bodies, demonstrating significant potential for water purification applications. This work offers valuable insights into the remote modulation of the electronic structure of confined Cu centers and proposes a potential approach for improving the catalytic activity of SACs for environmental applications.

Methods

Synthetic strategy of carbon nitride with different morphologies

Detailed information regarding the chemicals and materials is provided in Supplementary Note 1 of the Supporting information. The TCN support was fabricated following a previously reported method[54]. Specifically, urea (8 g), melamine (6 g), and ultrapure water (70 mL) were placed in a 100 mL Teflon-lined stainless-steel autoclave and stirred for 20 min. The resulting mixture was then subjected to hydrothermal treatment at 180℃ for 24 h. Afterwards, the precursor was thoroughly washed several times and dried. The dried precursor was subsequently heated to 550℃ at 2.3 ℃/min and kept for 4 h to obtain TCN. For comparison, BCN was prepared by directly heating melamine to 550°C at the same ramp rate (2.3 °C/min) and maintaining this temperature for 4 h. Under otherwise identical calcination conditions, FCN was synthesized by replacing melamine with urea as the precursor.

Synthetic strategy of Cu SACs

The CuTCN/C were synthesized by a one-step calcination method. In detail, TCN (0.25 g) and cupric acetylacetonate ($C_{10}H_{14}CuO_4$) (0.5 mmol) were mixed and ground in an agate mortar. The mixtures were transferred into a lidded ceramic crucible and subsequently heated in tube furnace at 550°C for 2 h under Ar atmosphere, with a heating rate of 2.5 °C/min. The obtained sample was then immersed in 1.5 M H_2SO_4 at 80°C for 12 h to remove Cu clusters and nanoparticles. Afterwards, the product was thoroughly washed with deionized water until the pH reached neutral, and then dried to obtain CuTCN/C. For comparison, CuBCN/C and CuFCN/C were prepared following the same procedure as CuTCN/C, except that TCN was replaced with BCN and FCN, respectively. CuTCN, FeTCN/C, and CoTCN/C was synthesized by replacing cupric acetylacetonate with $CuSO_4 \cdot 5H_2O$, ferrous acetylacetonate, and cobalt acetylacetonate, respectively. TCN/C was prepared by substituting cupric acetylacetonate with sodium acetylacetonate. To determine the optimal amount of cupric acetylacetonate, various CuTCN/C with different cupric acetylacetonate dosages (0.1, 0.25, 0.5, 1.0 mmol) were prepared and denoted as CuTCN/C-0.1, CuTCN/C-0.25, CuTCN/C, and CuTCN/C-1, respectively.

Degradation experiments

The catalytic oxidation experiments were carried out in a 150 mL beaker at room temperature. Specifically, the catalyst (3 mg) was dispersed into 100 ml of target pollutant solution (0.1 mM ACE) and stirred magnetically at 550 rpm for 30 min to achieve the adsorption/desorption equilibrium. Then, PMS (0.2 mM) was added to the above mixture solution to start the catalytic oxidation. After a certain interval, a 1.5 mL sample solution was withdrawn and immediately added with 20 μL $Na_2S_2O_3$ (0.5 M) to quench the PMS activation reactions. The initial pH values (before PMS addition) of the solution were adjusted by 0.1 M NaOH or HCl. All experiments were conducted in duplicates at least, and the mean values with standard deviations were reported. More details are provided in Supplementary material.

Data availability

The data generated in this study are provided within the article and the Supplementary Information/Source Data file. Data are available from the corresponding authors upon request. Source data are provided with this paper[55].

References

1. Yan, H. et al. Metal-carbon hybrid materials induced persulfate activation: Application, mechanism, and tunable reaction pathways. *Water Res.* **234**, 119808 (2023).
2. Parvulescu, V. I. et al. Recent Progress and Prospects in Catalytic Water Treatment. *Chem. Rev.* **122**, 2981-3121 (2022).
3. Hodges, B. C., Cates, E. L. & Kim, J.-H. Challenges and prospects of advanced oxidation water treatment processes using catalytic nanomaterials. *Nat. Nanotechnol.* **13**, 642-650 (2018).
4. Pei, J. et al. Non-metallic iodine single-atom catalysts with optimized electronic structures for efficient Fenton-like reactions. *Nat. Commun.* **16**, 800 (2025).
5. Zhao, Y. et al. Selective Degradation of electron-rich organic pollutants induced by CuO@Biochar: The key role of outer-sphere interaction and singlet oxygen. *Environ. Sci. Technol.* **56**, 10710-10720 (2022).
6. Liu, S. et al. Peroxydisulfate activation by sulfur-doped ordered mesoporous carbon: Insight into the intrinsic relationship between defects and $^1O_2$ generation. *Water Res.* **221**, 118797 (2022).
7. Zhou, Z. et al. Fe–Fe double-atom catalysts for murine coronavirus disinfection: nonradical activation of peroxides and mechanisms of virus inactivation. *Environ. Sci. Technol.* **57**, 3804-3816 (2023).
8. Zhao, X. & Zhang, Z. Heterogeneous peroxymonosulfate-based advanced oxidation mechanisms: new wine in old bottles? *Environ. Sci. Technol.* **59**, 5913-5924 (2025).

9. Ren, W. et al. Origins of electron-transfer regime in persulfate-based nonradical oxidation processes. *Environ. Sci. Technol* **56**, 78-97 (2022).

10. Xu, S. et al. Highly efficient peroxymonosulfate activation on electron-enriched ruthenium dual-atom sites catalysts for enhanced water purification. *Adv. Funct. Mater* **33**, 2308204 (2023).

11. Shang, Y. et al.. Single-atom catalysis in advanced oxidation processes for environmental remediation. *Chem. Soc. Rev.* **50**, 5281-5322 (2021).

12. Li, X. et al. Single cobalt atoms anchored on porous N-doped graphene with dual reaction sites for efficient fenton-like catalysis. *J. Am. Chem. Soc.* **140**, 12469-12475 (2018).

13. Yan, H. et al. Insight into the selective oxidation behavior of organic pollutants via Ni-N_4-C mediated electron transfer pathway. *Chem. Eng. J.* **473**, 145253 (2023).

14. Tian, Q. et al. Iron single-atom based double-reaction-center catalysis triggers internal-driven and external-driven pathways for green Fenton-Like chemistry. *Angew. Chem., Int. Ed.* **64**, e202503995 (2025).

15. Guo, J. et al. Fenton-like activity and pathway modulation via single-atom sites and pollutants comediates the electron transfer process. *Proc. Natl. Acad. Sci. USA* **121**, e2313387121 (2024).

16. Tian, H. et al. High durability of Fe–N–C single-atom catalysts with carbon vacancies toward the oxygen reduction reaction in alkaline media. *Adv. Mater.* **35**, 2210714 (2023).

17. Chen, F. et al. Single-atom iron anchored tubular g-C_3N_4 catalysts for ultrafast Fenton-like reaction: Roles of high-valency iron-oxo species and organic radicals. *Adv. Mater.* **34**, 2202891 (2022).

18. Jiang, X. et al. Precise coordination of high-loading Fe single atoms with sulfur boosts selective generation of nonradicals. *Proc. Natl. Acad. Sci. USA* **121** (2024).
19. Song, J. et al. Asymmetrically coordinated CoB_1N_3 moieties for selective generation of High-valence Co-oxo species via coupled electron–proton transfer in Fenton-like reactions. *Adv. Mater.* **35**, 2209552 (2023).
20. Yang, P. et al. Regulating the local electronic structure of copper single atoms with unsaturated B,O-coordination for selective $^1O_2$ generation. *ACS Catal.* **13**, 12414-12424 (2023).
21. Ren, S. et al. Transforming plastics to single atom catalysts for peroxymonosulfate activation: Axial chloride coordination intensified electron transfer pathway. *Adv. Mater.* **37**, 2415339 (2025).
22. Wu, Z. et al. Long-range interactions driving neighboring Fe–N_4 sites in Fenton-like reactions for sustainable water decontamination. *Nat. Commun.* **15**, 7775 (2024).
23. Zhang, L. et al. Deciphering the origin of higher shell coordination on single iron catalysts for resilient modulating persulfate oxidation into singlet oxygen pathway. *Adv. Funct. Mater* **35**, 2417441 (2025).
24. Zhu, G., Fan, X., Yu, Y., Liu, Y. & Quan, X. Regulating the electronic structure of Cu single-atom catalysts toward enhanced electro-Fenton degradation of organic contaminants via $^1O_2$ and •OH. *Environ. Sci. Technol.* **58**, 19545-19554 (2024).
25. Song, J. et al. Directional formation of reactive oxygen species via a non-redox catalysis strategy that bypasses electron transfer process. *Adv. Mater.* **36**, 2405832 (2024).
26. Dong, X. et al. Mineral modulated single atom catalyst for effective water treatment. *Adv.*

Funct. Mater. **32**, 2111565 (2022).

27. Wang, Z. et al. Cobalt single atoms anchored on oxygen-doped tubular carbon nitride for efficient peroxymonosulfate activation: Simultaneous coordination structure and morphology modulation. *Angew. Chem., Int. Ed.* **61**, e202202338 (2022).

28. Yin, K. et al. Pore modulation of single atomic Fe sites for ultrafast Fenton-like chemistry with amplified electron migration oxidation. *Water Res.* **268**, 122545 (2025).

29. Meng, Y. et al. Nanoconfinement steers nonradical pathway transition in single atom fenton-like catalysis for improving oxidant utilization. *Nat. Commun.* **15**, 5314 (2024).

30. Zhang, Z.-Q. et al. Nano-island-encapsulated cobalt single-atom catalysts for breaking activity-stability trade-off in Fenton-like reactions. *Nat. Commun.* **16,** 115 (2025).

31. Chen, T. et al. Robust Fe-N_4-C_6O_2 single atom sites for efficient PMS activation and enhanced $Fe^{IV} = O$ reactivity. *Nat. Commun.* 16, 2402 (2025).

32. Ya, Z. et al. Template-free synthesis of phosphorus-doped g-C_3N_4 micro-tubes with hierarchical core–shell structure for high-efficient visible light responsive catalysis. *Small* **19**, 2208254 (2023).

33. Li, H., Shan, C. & Pan, B. Fe(III)-doped g-C_3N_4 mediated peroxymonosulfate activation for selective degradation of phenolic compounds via high-valent iron-oxo species. *Environ. Sci. Technol.* **52**, 2197-2205 (2018).

34. Du, L., Gao, B., Xu, S. & Xu, Q. Strong ferromagnetism of g-C_3N_4 achieved by atomic manipulation. *Nat. Commun.* **14**, 2278 (2023).

35. Liu, B. et al. Novel nonradical oxidation of sulfonamide antibiotics with Co(II)-doped g-C_3N_4-activated peracetic acid: Role of high-valent cobalt–oxo species. *Environ. Sci.*

Technol. **55**, 12640-12651 (2021).

36. Cui, J. et al. Regulating the metal–support interaction: Double jump to reach the efficiency apex of the Fe–N_4-catalyzed fenton-like reaction. *ACS Catal.* **12**, 14954-14963 (2022).
37. Xiong, Y. et al. Single-atom Fe catalysts for Fenton-like reactions: Roles of different N species. *Adv. Mater.* **34**, 2110653 (2022).
38. Lin, J. et al. Tandem microplastic degradation and hydrogen production by hierarchical carbon nitride-supported single-atom iron catalysts. *Nat. Commun.* **15**, 8769 (2024).
39. Xu, F. et al. High-loaded single-atom Cu-N_3 sites catalyze hydrogen peroxide decomposition to selectively induce singlet oxygen production for wastewater purification. *Appl. Catal. B : Environ* **339**, 123075 (2023).
40. Yang, T. et al. Coordination tailoring of Cu single sites on C_3N_4 realizes selective CO_2 hydrogenation at low temperature. *Nat. Commun.* **12**, 6022 (2021).
41. Wan, Z. et al. Revealing intrinsic relations between Cu scales and radical/nonradical oxidations to regulate nucleophilic/electrophilic catalysis. *Adv. Funct. Mater.* **33**, 2212227 (2023).
42. Zhang, Y., Fan, J., Yang, B., Huang, W. & Ma, L. Copper–catalyzed activation of molecular oxygen for oxidative destruction of acetaminophen: The mechanism and superoxide-mediated cycling of copper species. *Chemosphere* **166**, 89-95 (2017).
43. Lin, H. et al. Degradation of bisphenol A by activating peroxymonosulfate with $Mn_{0.6}Zn_{0.4}Fe_2O_4$ fabricated from spent Zn-Mn alkaline batteries. *Chem. Eng. J.* **364**, 541-551 (2019).
44. Zhao, Z. et al. Enhanced interfacial electron transfer by asymmetric Cu-O_v-In sites on

In_2O_3 for efficient peroxymonosulfate activation. *Angew. Chem. Int. Ed.* **62**, (2023).

45. Li, F., Lu, Z., Li, T., Zhang, P. & Hu, C. Origin of the excellent activity and selectivity of a single-atom copper catalyst with unsaturated Cu-N_2 sites via peroxydisulfate activation: Cu(III) as a dominant oxidizing species. *Environ. Sci. Technol.* **56**, 8765-8775 (2022).
46. Tan, W. et al. Peroxymonosulfate activated with waste battery-based Mn-Fe oxides for pollutant removal: Electron transfer mechanism, selective oxidation and LFER analysis. *Chem. Eng. J.* **394**, 124864 (2020).
47. Ahn, Y.-Y. et al. Surface-loaded metal nanoparticles for peroxymonosulfate activation: Efficiency and mechanism reconnaissance. *Appl. Catal. B: Environ* **241**, 561-569 (2019).
48. Yan, H. et al. Insight into the selective oxidation behavior of organic pollutants via Ni-N_4-C mediated electron transfer pathway. *Chem. Eng. J.* **473**, 145253 (2023).
49. Ren, W. et al. Activation of peroxydisulfate on carbon nanotubes: Electron-transfer mechanism. *Environ. Sci. Technol.* **53**, 14595-14603 (2019).
50. Zhu, C. et al. Heterogeneous Fe-Co dual-atom catalyst outdistances the homogeneous counterpart for peroxymonosulfate-assisted water decontamination: New surface collision oxidation path and diatomic synergy. *Water Res.* **241**, 120164 (2023).
51. Liu, H.-Z. et al. Tailoring d-band center of high-valent metal-oxo species for pollutant removal via complete polymerization. *Nat. Commun.* **15**, 2327 (2024).
52. Fu, Z., Yang, B. & Wu, R. Understanding the activity of single-atom catalysis from frontier orbitals. *Phys. Rev. Lett.* **125**, 156001 (2020).
53. Pettersson, L. G. M. & Nilsson, A. A molecular perspective on the d-band model: Synergy between experiment and theory. *Top. Catal.* **57**, 2-13 (2014).

54. Wang, W. et al. Sulfur doped carbon quantum dots loaded hollow tubular g-C_3N_4 as novel photocatalyst for destruction of Escherichia coli and tetracycline degradation under visible light. *Chem. Eng. J.* **378**, 122132 (2019).

55. Yan, H. et al. Long-range electronic interactions of tubular single-atom Cu-N_3 catalysts for nanoconfined direct electron transfer oxidation. *Figshare* https://doi.org/10.6084/m9.figshare.31963329 (2026).

Funding

C.L. discloses support for the reseach of this work from the National Natural Science Foundation of China [52170161] and support for the publication of this work from the Hunan Natural Science Foundation [2024JJ2023]. S.L. discloses support for the reseach of this work from the Hunan Natural Science Foundation [2024JJ6138]. H.Y. discloses support for the reseach of this work from the Hunan Provincial Innovation Foundation for Postgraduate [CX20240440].

Acknowledgments

The authors have no non-funding acknowledgements to declare.

Author contributions

H.Y. and B.L. conceived the idea, performed the experiments, and writing this paper. S.L., X.Z., and M.Z. conducted characterizations and analyzed data; D.M. contributed to the DFT calculations; D.W., H.L. and X.D. assisted with data interpretation. C.L. supervised the project. All authors contributed to the discussion of the manuscript.

Competing interest

The authors declare no competing interests.

Figure legends

Fig. 1 Synthetic scheme and structural properties of CuTCN/C catalyst. a Schematic representation of the preparation pathway of CuTCN/C. **b–f** TEM images and corresponding EDS mappings of CuTCN/C. **g–j** SEM and **k–m** TEM images. **n** SAED pattern of CuTCN/C. **o-p** HAADF-STEM along with its enlarged intensity images of CuTCN/C.

Fig. 2 Chemical state and atomic structure characterization of the as-prepared catalysts. a Cu 2*p* XPS spectrum and Cu LMM Auger electron spectrum (inset) of CuTCN/C. **b** Normalized XANES spectra. **c** Cu *K*-edge FT-EXAFS spectra and **d** EXAFS fitting analyses in R-space and *k*-space (inset) of CuTCN/C. **e–i** WT-EXAFS contour plots of Cu foil, Cu_2O, CuO, CuPc, and CuTCN/C. Source data are provided as a Source Data file.

Fig. 3 Fenton-like catalytic performance, reactive intermediates identification and reaction process characterization. a ACE degradation efficiency. **b** Degradation efficiency and degradation kinetics under different quenching conditions. **c** EPR spectra of active species generated in CuTCN/C+PMS or PMS system. **d** In situ Raman spectra for CuTCN/C+PMS+ACE, CuTCN/C+PMS, PMS, and CuTCN/C systems. **e** In situ FT-IR spectra for CuTCN/C+PMS, PMS, and CuTCN/C systems. **f** OCP curves following sequential addition of PMS and ACE. **g** CA curves with/without ACE at different potentials. **h** Nonradical reaction mechanism in the CuTCN/C+PMS system. Error bars of **a** and **b** represent the standard deviation, obtained by repeating the experiment twice. Reaction conditions: [ACE]

= 0.1 mM, [catalyst] = 0.03 g/L, [PMS] = 0.2 mM. Source data are provided as a Source Data file. Source data are provided as a Source Data file.

Fig. 4 MD simulations and DFT calculations for elucidating the nanoconfinement effects and long-range interaction mechanism. a The PMS concentration distribution obtained from MD simulations and the MSD results show the PMS diffusion dynamics for different catalysts. **b** EIS of different catalysts. **c** Gibbs free energy diagram for PMS activation. The PDOS of **d** CuTCN and **e** CuTCN/C. **f** Correlation among the oxidation ability, PMS binding affinity, and *d*-band center of CuTCN and CuTCN/C. **g–h** The PDOS for Cu 3*d*, C 2*p* of doped C, and O 2*p* of PMS adsorbed on the Cu center. **i** Charge density difference for PMS adsorbed on CuTCN and CuTCN/C, where yellow indicates electron accumulation and cyan indicates electron depletion. Source data are provided as a Source Data file.

Fig. 5 Life cycle assessment (LCA) and practical application potential evaluation. a Relative environmental impact of the CuTCN+PMS, CuBCN/C+PMS, and CuTCN/C+PMS systems for treating 1 kg ACE in the Fenton-like process. **b** Cyclic ACE removal performance of CuTCN/C+PMS system. **c** ACE removal rate in the reactor. **d** Photograph of experimental device. **e, f** Photograph of CuTCN/C@PVDF membranes. **g** SEM of PVDF membrane surface and **h** CuTCN/C@PVDF membrane cross section. Error bars of **b** and **c** represent the standard deviation, obtained by repeating the experiment twice. Source data are provided as a Source Data file.

Editorial summary: Atomically dispersed catalysts that enable selective nonradical oxidation can overcome the short lifetimes and poor selectivity of radical-based water treatment processes. Here, the authors combine long-range electronic modulation with nanoconfinement by embedding isolated Cu–N_3 sites in carbon-doped tubular carbon nitride, demonstrating strong potential for water purification.

Peer review information: *Nature Communications* thanks Zhen-Yu Wu and the other, anonymous, reviewer(s) for their contribution to the peer review of this work. A peer review file is available.

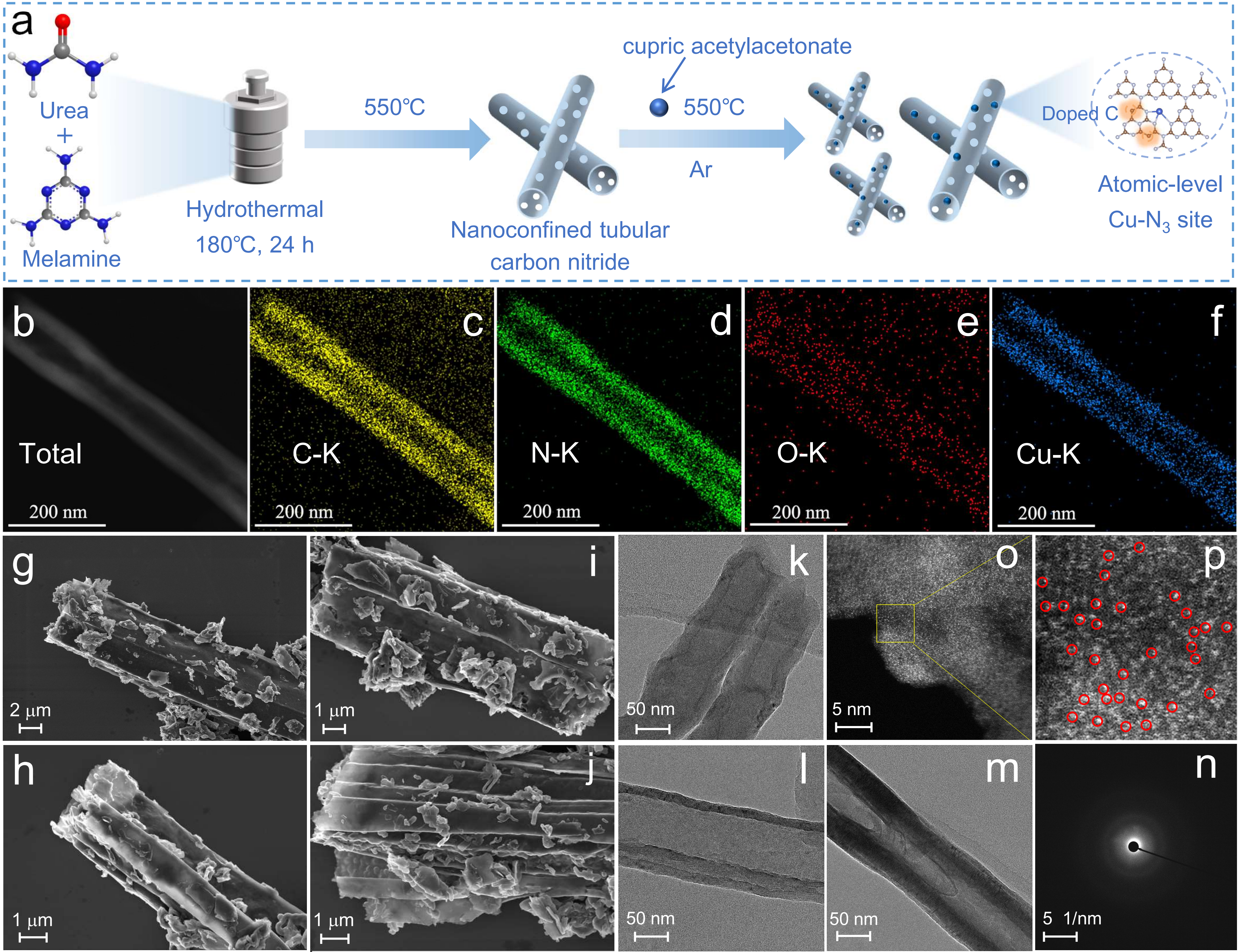
a
Urea
+
Melamine
Hydrothermal
180℃, 24 h
550℃
Nanoconfined tubular
carbon nitride
cupric acetylacetonate
550℃
Ar
Doped C
Atomic-level
Cu-N3 site
b
Total
200 nm
c
C-K
200 nm
d
N-K
200 nm
e
O-K
200 nm
f
Cu-K
200 nm
g
2 μm
i
1 μm
k
50 nm
o
5 nm
p
h
1 μm
j
1 μm
l
50 nm
m
50 nm
n
5 1/nm

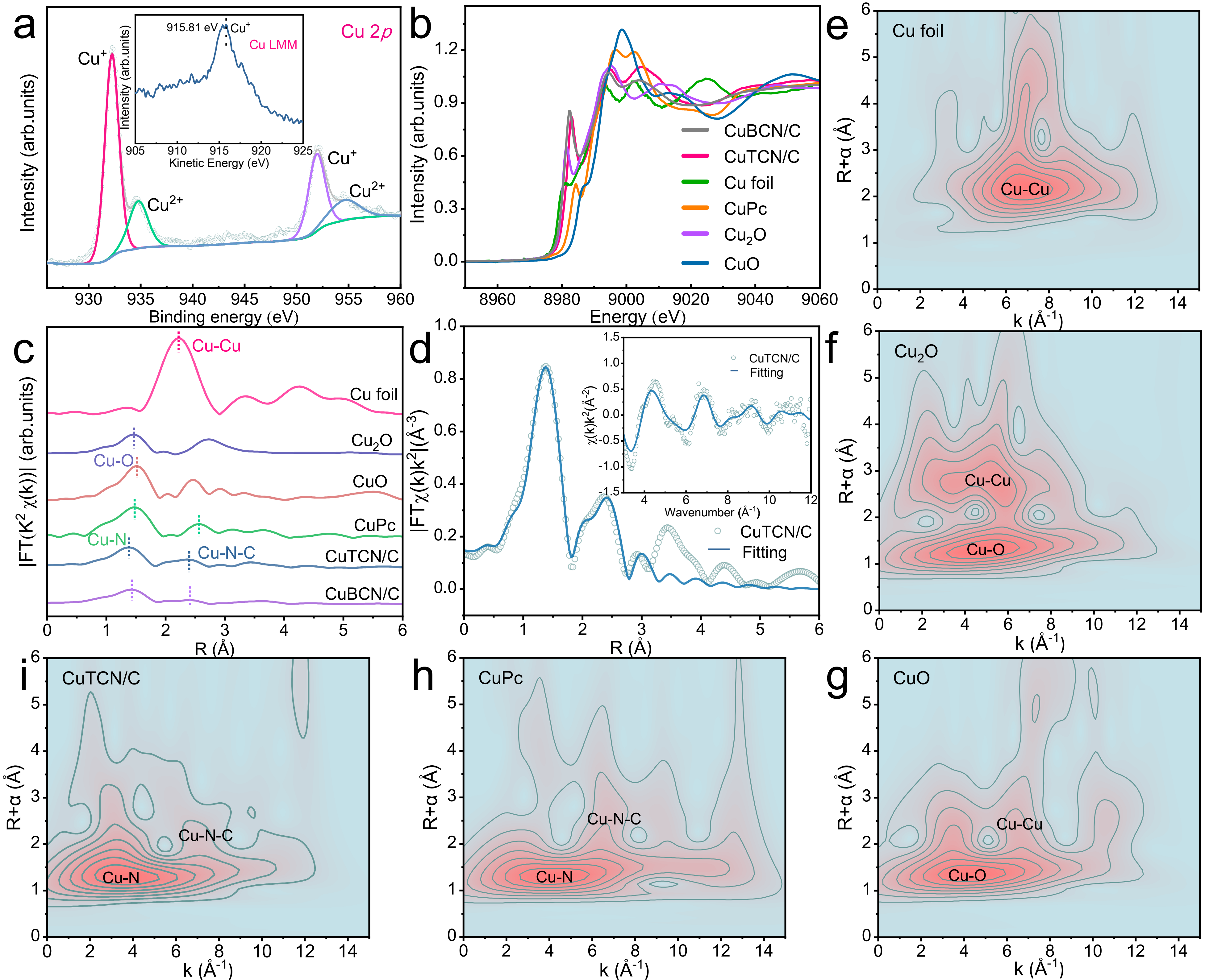
a
Cu 2p
Cu⁺
Cu²⁺
Cu⁺
Cu²⁺
915.81 eV
Cu⁺
Cu LMM
Intensity (arb.units)
905 910 915 920 925
Kinetic Energy (eV)
Intensity (arb.units)
930 935 940 945 950 955 960
Binding energy (eV)
b
CuBCN/C
CuTCN/C
Cu foil
CuPc
Cu2O
CuO
0.0 0.3 0.6 0.9 1.2
Intensity (arb.units)
8960 8980 9000 9020 9040 9060
Energy (eV)
e
Cu foil
Cu-Cu
R+α (Å)
k (Å⁻¹)
c
Cu-Cu
Cu foil
Cu2O
Cu-O
CuO
CuPc
Cu-N
Cu-N-C
CuTCN/C
CuBCN/C
|FT(K² χ(k))| (arb.units)
0 1 2 3 4 5 6
R (Å)
d
|FTχ(k)k²|(Å⁻³)
0.0 0.2 0.4 0.6 0.8 1.0
CuTCN/C
Fitting
χ(k)k²(Å⁻²)
Wavenumber (Å⁻¹)
CuTCN/C
Fitting
R (Å)
f
Cu2O
Cu-Cu
Cu-O
R+α (Å)
k (Å⁻¹)
i
CuTCN/C
Cu-N-C
Cu-N
R+α (Å)
k (Å⁻¹)
h
CuPc
Cu-N-C
Cu-N
R+α (Å)
k (Å⁻¹)
g
CuO
Cu-Cu
Cu-O
R+α (Å)
k (Å⁻¹)

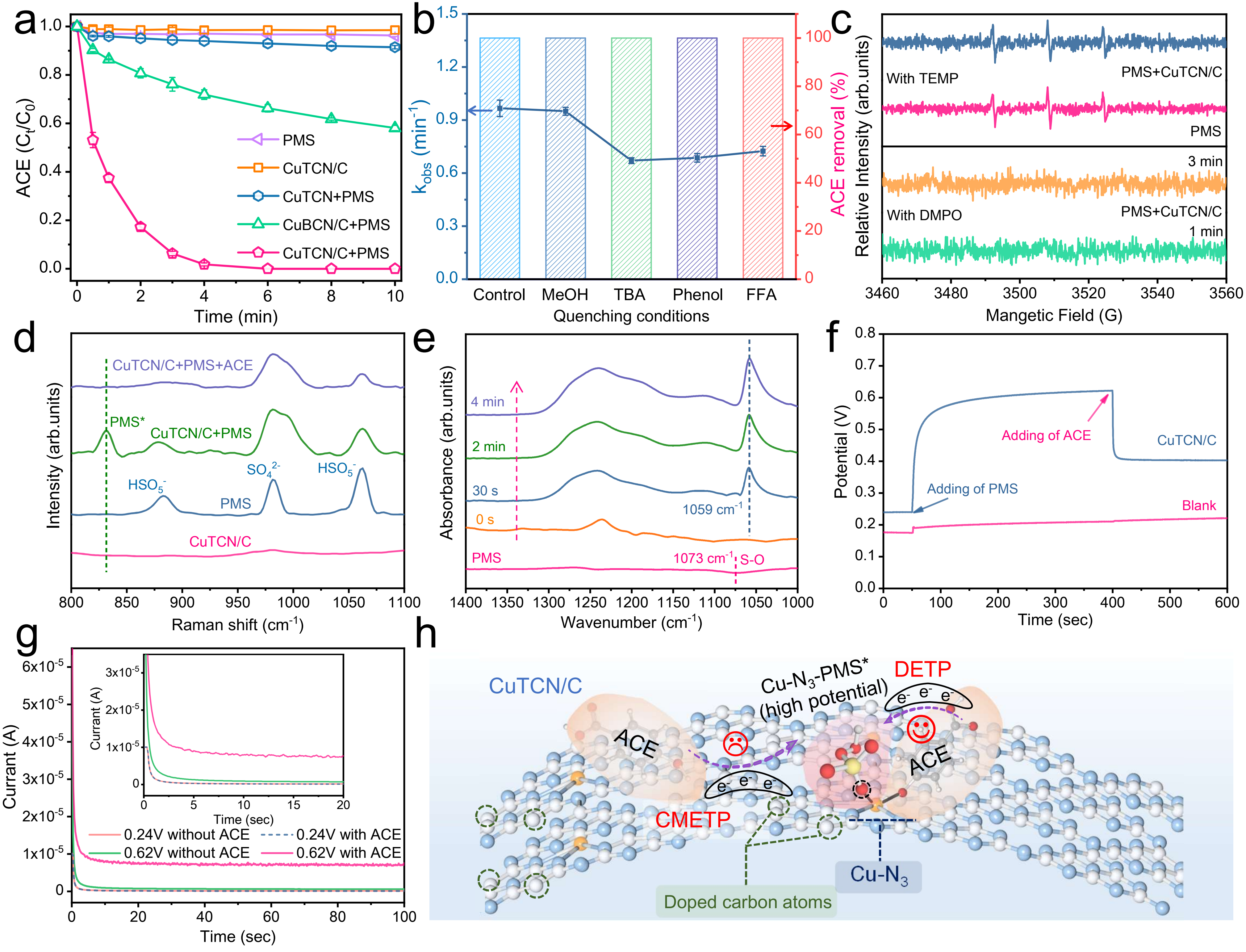
a
ACE (C_t/C_0)
Time (min)
PMS
CuTCN/C
CuTCN+PMS
CuBCN/C+PMS
CuTCN/C+PMS
b
k_{obs} (min^{-1})
ACE removal (%)
Control
MeOH
TBA
Phenol
FFA
Quenching conditions
c
Relative Intensity (arb.units)
With TEMP
PMS+CuTCN/C
PMS
3 min
With DMPO
PMS+CuTCN/C
1 min
Mangetic Field (G)
d
Intensity (arb.units)
CuTCN/C+PMS+ACE
PMS*
CuTCN/C+PMS
HSO_5^-
SO_4^{2-}
HSO_5^-
PMS
CuTCN/C
Raman shift (cm^{-1})
e
Absorbance (arb.units)
4 min
2 min
30 s
0 s
PMS
1059 cm^{-1}
1073 cm^{-1}
S-O
Wavenumber (cm^{-1})
f
Potential (V)
Adding of ACE
CuTCN/C
Adding of PMS
Blank
Time (sec)
g
Currant (A)
Currant (A)
Time (sec)
0.24V without ACE
0.24V with ACE
0.62V without ACE
0.62V with ACE
Time (sec)
h
CuTCN/C
ACE
Cu-N_3-PMS* (high potential)
DETP
ACE
CMETP
Cu-N_3
Doped carbon atoms

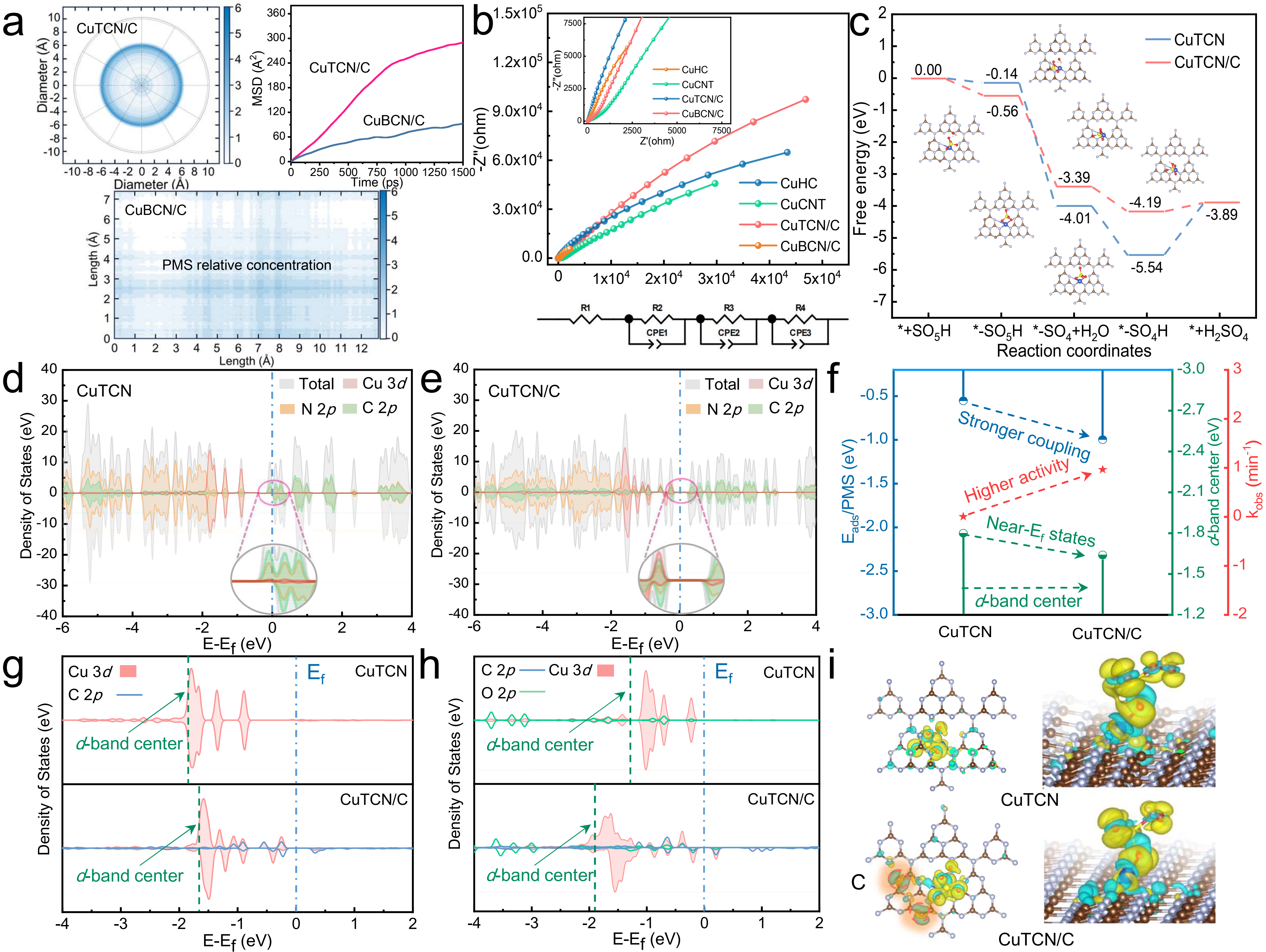
a
CuTCN/C
Diameter (Å)
Diameter (Å)
MSD (Å²)
Time (ps)
CuTCN/C
CuBCN/C
CuBCN/C
PMS relative concentration
Length (Å)
Length (Å)
b
-Z''(ohm)
Z'(ohm)
CuHC
CuCNT
CuTCN/C
CuBCN/C
R1
R2
R3
R4
CPE1
CPE2
CPE3
c
Free energy (eV)
CuTCN
CuTCN/C
0.00
-0.14
-0.56
-3.39
-4.01
-4.19
-5.54
-3.89
*+SO5H
*-SO5H
*-SO4+H2O
*-SO4H
*+H2SO4
Reaction coordinates
d
CuTCN
Total
Cu 3d
N 2p
C 2p
Density of States (eV)
E-Ef (eV)
e
CuTCN/C
Total
Cu 3d
N 2p
C 2p
Density of States (eV)
E-Ef (eV)
f
Eads/PMS (eV)
d-band center (eV)
kobs (min⁻¹)
Stronger coupling
Higher activity
Near-Ef states
d-band center
CuTCN
CuTCN/C
g
Cu 3d
C 2p
Ef
CuTCN
d-band center
CuTCN/C
d-band center
Density of States (eV)
E-Ef (eV)
h
C 2p
Cu 3d
O 2p
Ef
CuTCN
d-band center
CuTCN/C
d-band center
Density of States (eV)
E-Ef (eV)
i
CuTCN
C
CuTCN/C

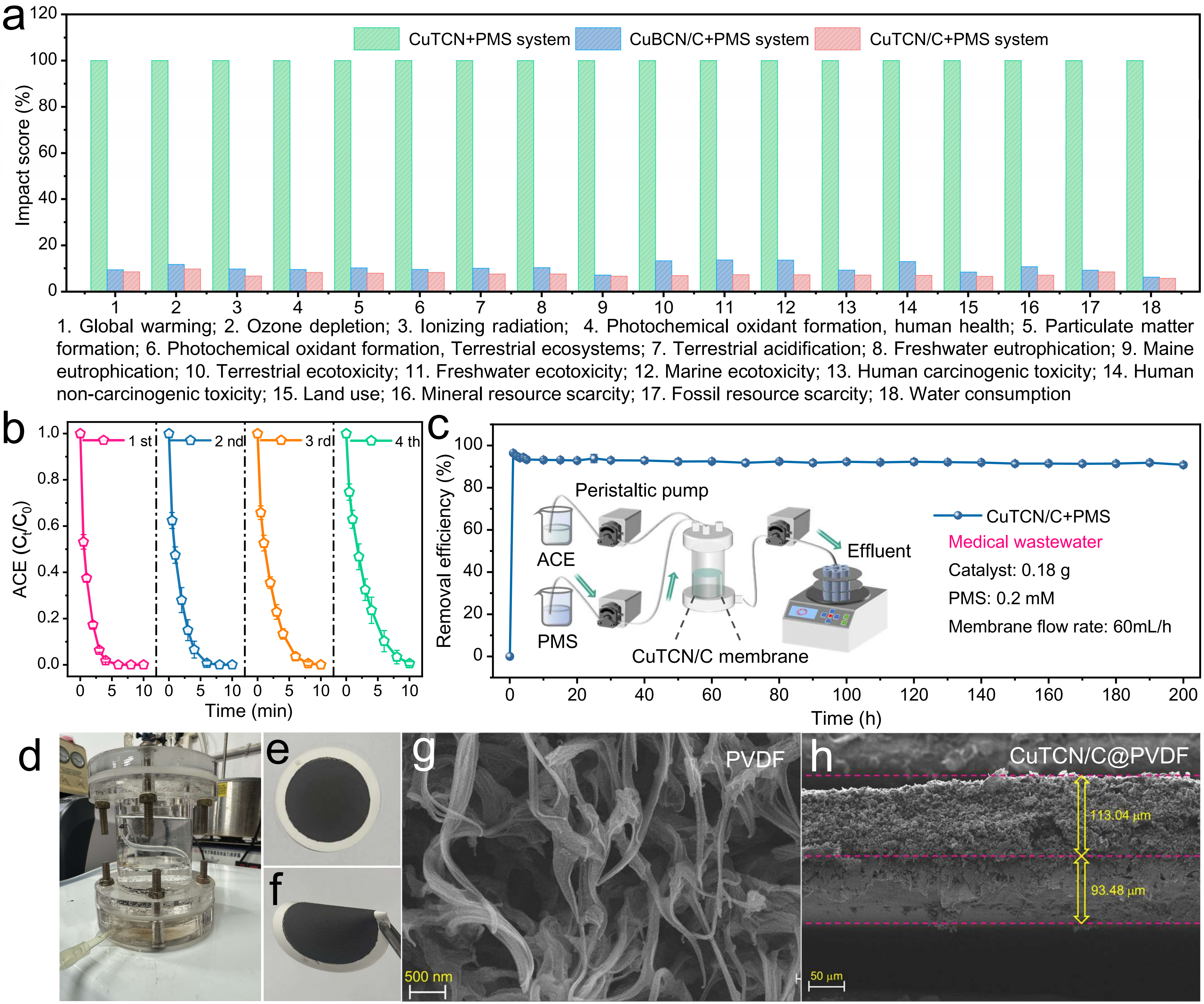
a
CuTCN+PMS system
CuBCN/C+PMS system
CuTCN/C+PMS system
Impact score (%)
0
20
40
60
80
100
120
1 2 3 4 5 6 7 8 9 10 11 12 13 14 15 16 17 18
1. Global warming; 2. Ozone depletion; 3. Ionizing radiation; 4. Photochemical oxidant formation, human health; 5. Particulate matter formation; 6. Photochemical oxidant formation, Terrestrial ecosystems; 7. Terrestrial acidification; 8. Freshwater eutrophication; 9. Maine eutrophication; 10. Terrestrial ecotoxicity; 11. Freshwater ecotoxicity; 12. Marine ecotoxicity; 13. Human carcinogenic toxicity; 14. Human non-carcinogenic toxicity; 15. Land use; 16. Mineral resource scarcity; 17. Fossil resource scarcity; 18. Water consumption
b
1 st
2 nd
3 rd
4 th
ACE (C_t/C_0)
0.0
0.2
0.4
0.6
0.8
1.0
0 5 10 0 5 10 0 5 10 0 5 10
Time (min)
c
Removal efficiency (%)
0
20
40
60
80
100
Peristaltic pump
ACE
PMS
Effluent
CuTCN/C membrane
CuTCN/C+PMS
Medical wastewater
Catalyst: 0.18 g
PMS: 0.2 mM
Membrane flow rate: 60mL/h
0 20 40 60 80 100 120 140 160 180 200
Time (h)
d
e
f
g
PVDF
500 nm
h
CuTCN/C@PVDF
113.04 μm
93.48 μm
50 μm